SPACE TELESCOPE SCIENCE INSTITUTE
Operated for NASA by AURA

Instrument Science Report WFC3 2009-30

WFC3 SMOV Proposal 11451: The Photometric Performance and Calibration of WFC3/IR

J. S. Kalirai, J. MacKenty
R. Bohlin, T. Brown, S. Deustua, R. A. Kimble, A. Riess, and the WFC3 Team
November 18, 2009

Abstract

We present the first on-orbit observations to characterize the photometric performance of the infrared (IR) camera on WFC3, based on data collected during the Servicing Mission Orbital Verification 4 Phase (SMOV4) shortly after the installation of the WFC3 instrument on HST. The photometric zero points and stability of the detector are measured in all 15 IR filters, using two different HST spectrophotometric standards; the hot white dwarf star GD 153 and the cooler solar analog P330E. The measured counts of these stars are calculated from dithered, high signal-to-noise imaging observations. We find that the total system throughput of WFC3/IR is better than expected from the Thermal Vacuum (TV3) testing campaign, exhibiting efficiency gains of $\sim$*10 – 15% at all wavelengths. Repeat observations in all 15 filters are obtained at time intervals of 1 day, 1 week, and 1 month, and demonstrate that the throughput is stable to* $<$*1% in the medium and wide band filters. We update the Exposure Time Calculator (ETC) with these preliminary results by fitting a smooth curve (3rd order polynomial) to the ratios of the efficiency gains over previous predictions, in the medium and wide band filters. This polynomial is multiplied into the SYNPHOT throughput routines. We calculate photometric zero points for the IR camera, factoring in the new on-orbit sensitivity measurements, in three photometric systems, STMAG, ABMAG, and VEGAMAG. A much more detailed Cycle 17 calibration plan, including observations targeting additional primary standards, begins in October 2009.*

1. The New WFC3 Camera on HST

The Wide Field Camera 3 (WFC3) was installed on the Hubble Space Telescope (HST) in May 2009 as a part of Servicing Mission 4. The instrument includes both a high resolution UV/optical

imaging camera and an infrared (IR) detector, and has quickly emerged as the workhorse instrument on HST. In Cycle 17, more than 50% of the allocated orbits on HST will be executed with WFC3. The photometric performance of the UVIS camera is discussed in Kalirai et al. (2009a), here we focus on the IR detector.

The IR channel of WFC3 offers imaging over a wavelength range extending from 9000 – 17000 Å. The detector is an HgCdTe array with a field of view of 123 × 136 arcseconds, and has a pixel scale of 0.13 arcseconds. Both imaging and spectroscopic modes are available through 15 filters (5 wide band, 4 medium band, and 6 narrow band) and two grisms (see Table 1).

In this document, we present the results from the WFC3 calibration program CAL11451 (Kalirai & Brown), which is aimed at characterizing the photometric performance of the IR channel through observations obtained during the three month period following SM4 (e.g., the Servicing Mission Orbital Verification 4 – SMOV4). This program targets two bright HST spectrophotometric standard stars with very different temperatures, the hot white dwarf star GD 153 and the solar analog P330E.

In the next section, we summarize the ground calibration of WFC3/IR during several testing campaigns prior to launch, and then describe the on-orbit observations from CAL11451. We briefly summarize the processing steps of the raw data through the WFC3 pipeline and the technique adopted to measure the count rate of each star through aperture photometry. These measurements are next compared to the predicted counts from the Exposure Time Calculator (ETC), which convolves the total system throughput with the absolute flux calibration of these standards. This comparison demonstrates that the WFC3/IR system throughput was underestimated in the ground tests, and requires an overall upward sensitivity adjustment of $\sim$10 – 15%. We outline the method used to implement this change for current and future users, and calculate photometric zero points for WFC3/IR in several photometric systems. From here on, we refer to these predictions as counts measured in the STSDAS package SYNPHOT, which is the engine behind the ETC.

Finally, we discuss the scientific implication of these results as they relate to users wishing to undertake specific observations with HST. Given both the much higher sensitivity and larger field of view compared to previous HST imaging cameras in the near IR, WFC3 will be the preferred instrument for efficiently addressing many of the key scientific research problems in astronomy today.

2. Thermal Vacuum Testing of the WFC3 IR Detector

The system throughput of the IR camera on WFC3 was measured in three extensive Thermal Vacuum (TV) campaigns. These tests were carried out at NASA/GSFC using an optical stimulus called "CASTLE". The "CASTLE" system produces point-like images at the focal plane of the detector with a high signal, flux-calibrated monochromatic light source, therefore allowing the resulting throughput to be measured with standard aperture photometry. The detector in the first

Table 1: WFC3/IR Filter Characteristics

Filter	Pivot λ (Å)	Width λ (Å)[a]
F098M	9829.3	1694.8
F105W	10489.5	2923.0
F110W	11414.0	5034.0
F125W	12459.0	3015.0
F126N	12582.6	118.3
F127M	12736.4	687.9
F128N	12833.0	135.4
F130N	13006.2	132.8
F132N	13190.4	130.7
F139M	13838.0	645.8
F140W	13921.0	3990.0
F153M	15333.1	687.8
F160W	15405.2	2878.8
F164N	16451.3	174.8
F167N	16672.6	171.6
G102	(10250)	2500
G141	(14100)	6000

[a]See WFC3 Instrument Handbook (IHB) for more details.

testing campaign in 2004 (IR2; FPA064) was not substrate thinned and, therefore, was susceptible to elevated dark rates from cosmic ray impacts. The total system throughput with this detector was 15% lower than expected, as discussed in Brown, Reid, & Figer (2005). During the second TV campaign in 2007, a substrate thinned detector (IR1; FPA129) replaced IR2. The quantum efficiency (QE) of this detector was measured at the Detector Characterization Laboratory (DCL) to be significantly higher than IR2. Relative to the new expectations, the second TV tests of IR1 exhibited a measured deficiency in the throughput that varied smoothly from 2 – 20% going from blue to red wavelengths (Brown 2007).

In the latest TV3 tests, a much superior IR detector replaced IR1 and was chosen as the flight detector. The quantum efficiency of the new detector (IR4; FPA165) was measured at DCL to be significantly higher than IR1. The TV3 tests of IR4 indicated that the system throughput exceeds the already high expectations by 2 – 8% (Brown 2008). These findings may suggest that the QE of the first two detectors was overestimated by the DCL, and that of the flight detector was underestimated. The measured differences could also represent errors in the components of the "CASTLE" flux calibration, such as the optical stimulus or the photomultiplier tubes.

The current characterization of the overall WFC3/IR system throughput, built into SYNPHOT, results from the spring 2008 TV3 calibration discussed above (see Brown 2008 for details). The full model that yields the expected SYNPHOT counts for a given observational setup includes a contribution from the following components: the HST Optical Telescope Assembly (OTA), pickoff mirror, reflectivity of the channel select mechanism, filter throughput, detector window, QE of the

detector from DCL, and a correction factor based on the throughput gains seen in TV3 relative to expectations. The throughputs for each of these components were compiled from a number of sources including the Goddard Space Flight Center, Detector Characterization Laboratory (DCL), and Ball Aerospace (T. Brown, private communication).

3. SMOV4 Observations

The data set from the SMOV4 CAL11451 proposal represents the first WFC3/IR on-orbit imaging observations of stars with well known absolute fluxes. The primary goal of this analysis is to measure the counts of these stars and to compare to the predicted counts from the well understood spectral energy distribution, thereby establishing the true on-orbit throughput of the WFC3/IR detector in all filters. This can be characterized by the photometric zero points of the filters, which represent the magnitudes of a star-like object that produces one count per second within a given aperture. Our specific goal is to measure these zero points to an accuracy of a few percent with these observations. A secondary goal from these observations is to monitor the system throughput for temporal variations over the course of a month.

The three primary HST spectrophotometric standards used by previous/current instruments are the hot DA (hydrogen atmosphere) white dwarfs G191-B2B ($V = 11.77$; $H = 12.66$), GD 153 ($V = 13.35$; $H = 14.19$), and GD 71 ($V = 13.03$; $H = 13.86$). The optical spectrum of these stars exhibit only pressure broadened Balmer lines. Each of these stars has been observed with STIS, ACS, WFPC2, and NICMOS, and the resulting data has been analyzed and discussed in several papers, Bohlin, Colina, & Finley (1995); Bohlin (1996); Bohlin (2000); Bohlin, Dickinson, & Calzetti (2001); Bohlin (2007a). The Balmer absorption lines of these stars, as measured from the ground, have been modeled to yield the fundamental properties of each of the three white dwarfs (e.g., temperature and surface gravity – see e.g., Bergeron, Saffer, & Liebert 1992; Finley, Koester, & Basri 1997), thereby allowing the construction of a model out to IR wavelengths (Bohlin 2000). These models have residuals with respect to the STIS spectra that are better than 1%, indicating a superb absolute flux calibration (even in the near IR). Therefore, the predicted counts from convolving our instrument throughput with the model spectrum of either of these three stars yields a very accurate calibration.

As the three primary white dwarf standards are all hot stars, a cooler spectrophotometric standard is often used for the calibration of near IR instruments (e.g., NICMOS). The most popular non-WD standard for HST has been the G0V solar analog P330E ($V = 13.00$; $H = 11.48$). Although P330E is both a more common IR standard (primary standard for NICMOS imaging) and brighter in the IR bands than any of the white dwarfs, the star is not necessarily a better standard. P330E is one of several solar analogs and the comparison of fluxes from these stars differ at the several percent level (e.g., Bohlin 2007b; Colina & Bohlin 1997). In the IR, models of the Sun itself do not agree with the measured fluxes by up to 5%. These differences may be related to magnetic activity in the atmospheres of such stars, which vary in unpredictable ways in different stars. Additionally,

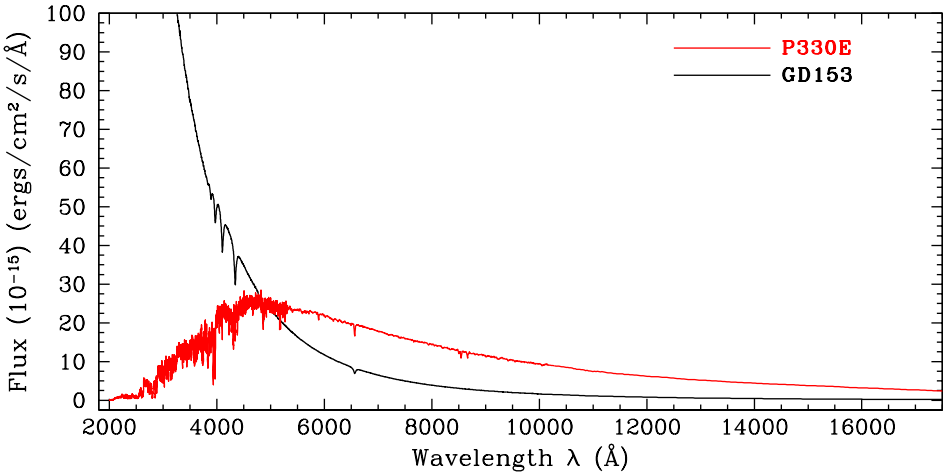

Fig. 1.— *The HST/STIS and NICMOS spectra of both GD 153 (black) and P330E (red). GD 153 show a smooth continuum with hydrogen Balmer lines (DA stars) in the optical and P330E exhibits a solar-like spectrum that is brighter than GD 153 at near IR wavelengths.*

the models for such stars suffer from poor atomic line data and uncertainties in abundances.

For the WFC3/IR calibration in SMOV4, we have observed both the hot white dwarf GD 153 *and* the solar analog P330E. The comparison of the system throughput, as derived from each of the standards, can possibly help shed light on some of the uncertainties listed above. Additionally, as the slope of the spectral energy distribution of the two stars is very different, the true bandpasses of the WFC3/IR filters can be tested. The observational setup includes four epochs of identical measurements over a 1 month period (initial, 1 day, 7 days, and ∼30 days). Both stars are exposed in all WFC3/IR filters using a combination of RAPID sequences (all filters) and SPARS10 sequences (narrow and medium band filters), to ensure a high signal-to-noise detection in each individual exposure (the S/N is $\gtrsim$100 in most observations). The 128 × 128 pixel subarray is used to reduce overheads (the subarray is centered on the IR detector) and all observations were obtained at two positions on the subarray separated by ∼5 pixels with a non-integer dither pattern. A log of these observations is provided in Table 2.

The combined STIS and NICMOS spectra of both GD 153 and P330E are displayed in Figure 1; both SEDs are from the STScI CALSPEC webpage (gd153_stisnic_002.fits and p330e_stisnic_002.fits).[1]

[1] `http://www.stsci.edu/hst/observatory/cdbs/calspec.html`, see Bohlin, Dickinson, & Calzetti (2001) and references therein for more information.

Table 2: WFC3/IR SMOV4 Photometric Calibration Observations

Target	Filters	Sequence[a]	Orbits
Visit 11 – 2009-07-13			
P330E	F098M, F105W, F110W, F125W, F126N	RAPID	1
	F127M, F128N, F130N, F132N, F139M		
	F140W, F153M, F160W, F164N, F167N		
	F126N, F128N, F130N, F132N, F164N, F167N	SPARS10	
Visit 12 – 2009-07-14			
P330E	F098M, F105W, F110W, F125W, F126N	RAPID	1
	F127M, F128N, F130N, F132N, F139M		
	F140W, F153M, F160W, F164N, F167N		
	F126N, F128N, F130N, F132N, F164N, F167N	SPARS10	
Visit 13 – 2009-07-21			
P330E	F098M, F105W, F110W, F125W, F126N	RAPID	1
	F127M, F128N, F130N, F132N, F139M		
	F140W, F153M, F160W, F164N, F167N		
	F126N, F128N, F130N, F132N, F164N, F167N	SPARS10	
Visit 14 – 2009-08-13			
P330E	F098M, F105W, F110W, F125W, F126N	RAPID	1
	F127M, F128N, F130N, F132N, F139M		
	F140W, F153M, F160W, F164N, F167N		
	F126N, F128N, F130N, F132N, F164N, F167N	SPARS10	
Visit 21 – 2009-07-13			
GD 153	F098M, F105W, F110W, F125W, F126N	RAPID	1
	F127M, F128N, F130N, F132N, F139M		
	F140W, F153M, F160W, F164N, F167N		
	F126N, F128N, F130N, F132N, F164N, F167N	SPARS10	
	F127M, F139M, F153M	SPARS10	
Visit 22 – 2009-07-14			
GD 153	F098M, F105W, F110W, F125W, F126N	RAPID	1
	F127M, F128N, F130N, F132N, F139M		
	F140W, F153M, F160W, F164N, F167N		
	F126N, F128N, F130N, F132N, F164N, F167N	SPARS10	
	F127M, F139M, F153M	SPARS10	
Visit 23 – 2009-07-21			
GD 153	F098M, F105W, F110W, F125W, F126N	RAPID	1
	F127M, F128N, F130N, F132N, F139M		
	F140W, F153M, F160W, F164N, F167N		
	F126N, F128N, F130N, F132N, F164N, F167N	SPARS10	
	F127M, F139M, F153M	SPARS10	
Visit 24 – 2009-08-11			
GD 153	F098M, F105W, F110W, F125W, F126N	RAPID	1
	F127M, F128N, F130N, F132N, F139M		
	F140W, F153M, F160W, F164N, F167N		
	F126N, F128N, F130N, F132N, F164N, F167N	SPARS10	
	F127M, F139M, F153M	SPARS10	

[a]The calwf3 pipeline performs an "up-the-ramp" fitting of the multiple non-destructive reads within each sample sequence. The output of this is a count rate (e.g., $e^- s^{-1}$), with the exact number of reads (and therefore the exposure time) varying from exposure to exposure depending on where/if saturation occurred.

4. Data Processing and Aperture Photometry

The raw images were retrieved from the Multimission Archive at Space Telescope (MAST) and processed with the IRAF/STSDAS pipeline program calwf3. The steps performed included a bias, dark, and flat field correction to the raw data, yielding the processed _flt images on which we perform photometry. Each of the non-destructive reads in the multiple samples are "up-the-ramp" fitted to convert the counts to count rates. This fitting also efficiently flags and removes cosmic rays detected on any individual read. The observations obtained in this program represented some of the first IR external exposures with WFC3, and so the data were reprocessed several times to reflect updated calibration files as more on-orbit data became available. The quality of the bias and flat will be improved over time and thus these data are still not optimally reduced. However, because the signal from the stellar standards is high, any future changes in the count rates should be <1%. Detailed information on each of the data reduction steps within calwf3 is presented in the WFC3 Data Handbook,
`http://www.stsci.edu/hst/wfc3/documents/handbooks/currentDHB/WFC3_longdhbcover`.

We performed aperture photometry on the _flt images using the DAOPHOT program (Stetson 1987; 1994). The counts were measured in 12 apertures with radii of 0.10 to 2.00 arcseconds (0.77 to 15.4 pixels), chosen to match the available options in the WFC3 ETC (i.e., 0.10, 0.15, 0.20, 0.25, 0.30, 0.40, 0.50, 0.60, 0.80, 1.00, 1.50, and 2.00 arcseconds). The sky was calculated as the modal value in an annulus extending from 2.6 to 5.2 arcseconds (i.e., 20 – 40 pixels).

The first three epochs of this program (e.g., Visits 11, 12, and 13 for P330E and Visits 21, 22, and 23 for GD 153 – see Table 2) were executed prior to an update that corrected a known gross offset in the absolute pointing accuracy of WFC3. Given that the magnitude of the astrometric offset was only 5 – 6 arcseconds, most calibration and science programs were unaffected. However, the 128 × 128 pixel subarray only subtends a total angular size of 16.6 arcseconds, and therefore the standard star was offset towards the corner of the subarray. In all observations, the star was located at least 2.7 arcseconds (21 pixels) from the edge of the field of view, and typically was ∼3.2 arcseconds from the edge. Therefore, none of our apertures are truncated due to this offset. Furthermore, the enclosed energy curves for WFC3/IR indicate that the flux at 2 arcseconds is >97% of the total flux, in all filters. As mentioned above, our sky measurement is nominally set to a large annulus extending from 2.6 to 5.2 arcseconds, however the annulus is truncated on the first three visits of each star. The pixels outside the bounds of the image towards the corner were simply ignored and the modal sky value was calculated from those pixels that fell on the image.

5. Aperture Corrections

The enclosed energy curves for the five wide band filters on WFC3/IR are displayed in Figure 2, as calculated from a model of the instrument. This model is found to agree nicely with the on-orbit measurements in the IR, as described in the results of the CAL11439 proposal (Hartig & Dressel

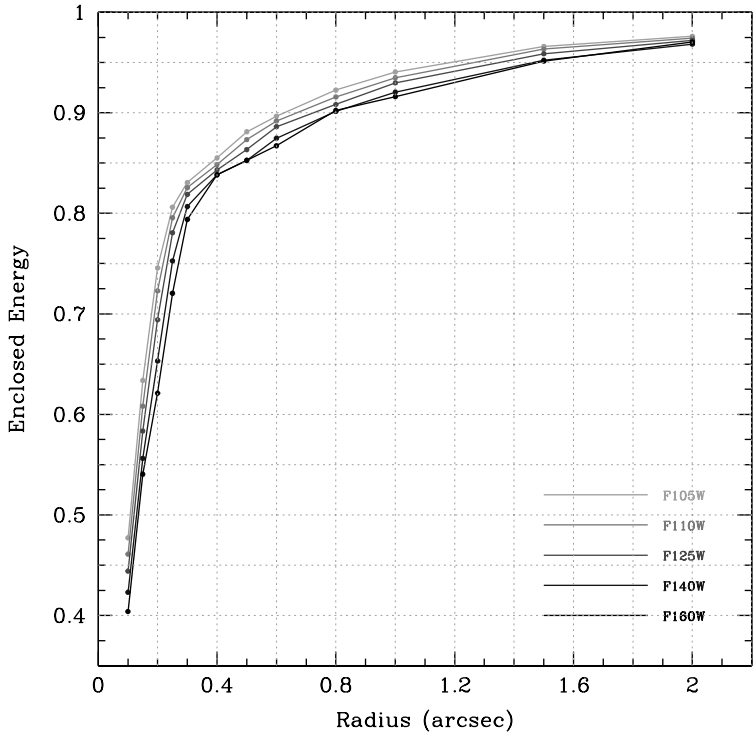

Fig. 2.— *The enclosed energy curves in the five broadband filters on WFC3/IR, from a model of the instrument. These model curves are found to be in excellent agreement with on-orbit measurements (see Hartig & Dressel 2009) and can be used to scale the total counts in an infinite aperture from SYNPHOT to the counts in a finite size aperture.*

2009). The measured flux for an aperture with $R = 2.0$ arcseconds is estimated to be $\gtrsim$97% of the total flux, in all filters. These aperture corrections (in the form of enclosed energy fractions) are presented in Table 3 and are used to scale the expected total counts from SYNPHOT (e.g., for an infinite aperture) to the counts in a given aperture in the comparisons that follow.[2]

6. Photometric Stability

The SMOV4 observations of P330E and GD 153 were all collected over a small area of the WFC3/IR detector and over a short temporal baseline of 1 month. These data are therefore not ideally suited to characterize the spatial and temporal stability of the instrument. Nevertheless, we illustrate the comparison of the counts measured on all eight of the individual exposures in Figure 3 (e.g., two dithers at four epochs). The black points illustrate the higher signal-to-noise observations

[2]The observations in this proposal were used to calculate the specific enclosed energy fractions that were applied, but these are found to agree nicely with the new model corrections in Table 3 (from Hartig & Dressel 2009).

Table 3: WFC3/IR On-Orbit Enclosed Energy Fractions

Radius (“)	0.8 μm	0.9 μm	1.0 μm	1.1 μm	1.2 μm	1.3 μm	1.4μm	1.5 μm	1.6 μm	1.7μm
0.10	0.549	0.524	0.502	0.484	0.468	0.453	0.438	0.426	0.410	0.394
0.15	0.714	0.685	0.653	0.623	0.596	0.575	0.558	0.550	0.539	0.531
0.20	0.794	0.780	0.762	0.739	0.712	0.683	0.653	0.631	0.608	0.590
0.25	0.827	0.821	0.813	0.804	0.792	0.776	0.756	0.735	0.708	0.679
0.30	0.845	0.838	0.833	0.828	0.822	0.816	0.808	0.803	0.789	0.770
0.40	0.876	0.869	0.859	0.850	0.845	0.841	0.838	0.840	0.836	0.832
0.50	0.894	0.889	0.884	0.878	0.868	0.858	0.852	0.854	0.850	0.848
0.60	0.913	0.904	0.897	0.893	0.889	0.883	0.875	0.870	0.863	0.859
0.80	0.936	0.929	0.924	0.918	0.909	0.903	0.900	0.903	0.900	0.895
1.00	0.951	0.946	0.941	0.935	0.930	0.925	0.920	0.917	0.912	0.909
1.50	0.969	0.967	0.965	0.963	0.959	0.954	0.951	0.952	0.948	0.943
2.00	0.977	0.976	0.975	0.973	0.972	0.969	0.967	0.970	0.967	0.963

in medium and wide band filters and the grey points represent the narrow band observations, where all ratios have been calculated with respect to the mean counts in the respective group. Almost all of the individual P330E observations in the medium and wide band filters are consistent with the mean counts at the 2% level, with a formal standard deviation of 0.89%. For GD 153, the scatter is slightly larger and the standard deviation is 1.03%. As the uncertainties in the individual count statistics are $\lesssim$1%, these observations indicate that the instrument is stable over the limited range of parameters space being tested.

As already discussed, the calibration reference files (e.g., biasses and flats) used in this data reduction will improve over time leading to a more accurate calibration. Also, the photometry presented here has not been corrected for relative variations in the areas of pixels across our subarray, something that will soon be available with the new WFC3 geometric distortion solution (Khozurina-Platais et al. 2009). A preliminary analysis of the uniformity of the flat field in the IR suggests an RMS scatter of 3% over the entire field of view, however this will improve with future removal of instrumental effects (CAL11453 – Hilbert et al. 2009).

7. Absolute WFC3/IR Throughput

A measurement of the absolute throughput of WFC3/IR is of fundamental importance to provide users of HST accurate information on which instrument is best suited for a particular science case. The throughput also provides photometric zero point information, and, therefore, a convenient means to translate the measured count rate of a given object into a magnitude (see Section 8). Prior to this work, the photometric information that is embedded in the headers of WFC3/IR images comes from the calibration in TV3. As those analysis indicated a gain of 2 – 8% in the total system throughput over expectations, a new correction term was created in SYNPHOT.

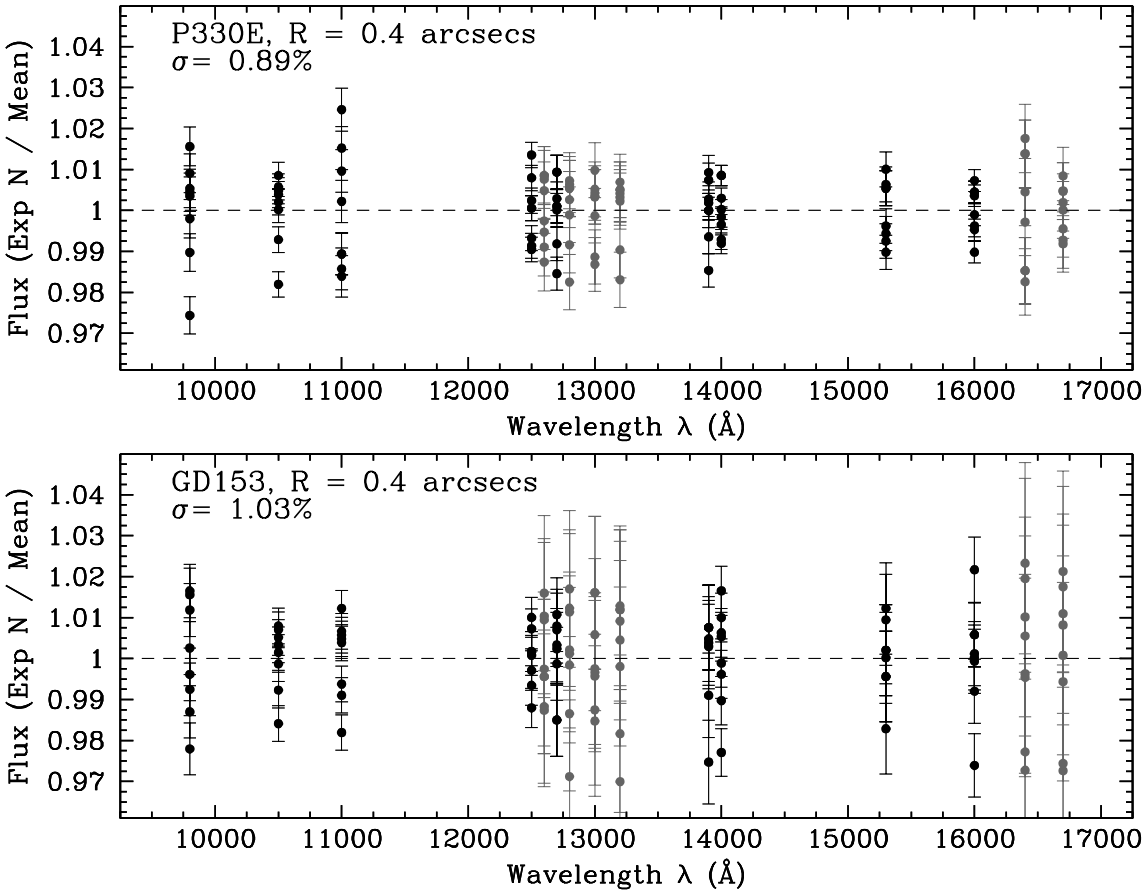

Fig. 3.— *The photometric stability of WFC3/IR, as measured by comparing the ratio of counts on all eight individual exposures in our program with the mean counts, for each of the two spectrophotometric standards P330E and GD 153. The eight individual exposures for each star represent the two dither patterns in each of the four visits. The comparison is presented for photometry measured in an intermediate aperture of R = 0.4 arcseconds. The black points illustrate the measurements in medium and wide band filters and the grey points represent the narrow-band filters. For the former, the standard deviation in the photometry is* $\lesssim$*1% across all filters.*

This correction term acts as an additional throughput table to yield the correct counts based on the TV3 calibration (applied in SYNPHOT in October 2009).

We calculated the final count rate of both P330E and GD 153 by averaging together all eight of the individual exposures of each star, in each filter (e.g., the two dither positions and the four epochs). The default aperture for the photometry is taken be $R = 0.4$ arcseconds. Next, we use the SYNPHOT package to predict the count rate of these stars in all filters, and scale these to 0.4 arcseconds based on the enclosed energy curves (see Figure 2 and Table 3). The SYNPHOT calculation involves a convolution between the total WFC3/IR throughput, including the TV3

correction factor, and the spectrum of the star. For P330E, the spectrum is a combined STIS and NICMOS spectrum of the star, as described in Bohlin (2007b). For GD 153, the spectrum is a model fit to the Balmer lines of the white dwarf, which agrees within 1% of the STIS + NICMOS spectrum of the star (see Finley, Koester, & Basri 1997; Bohlin 2000; Bohlin, Dickinson, & Calzetti 2001; Bohlin 2007b).

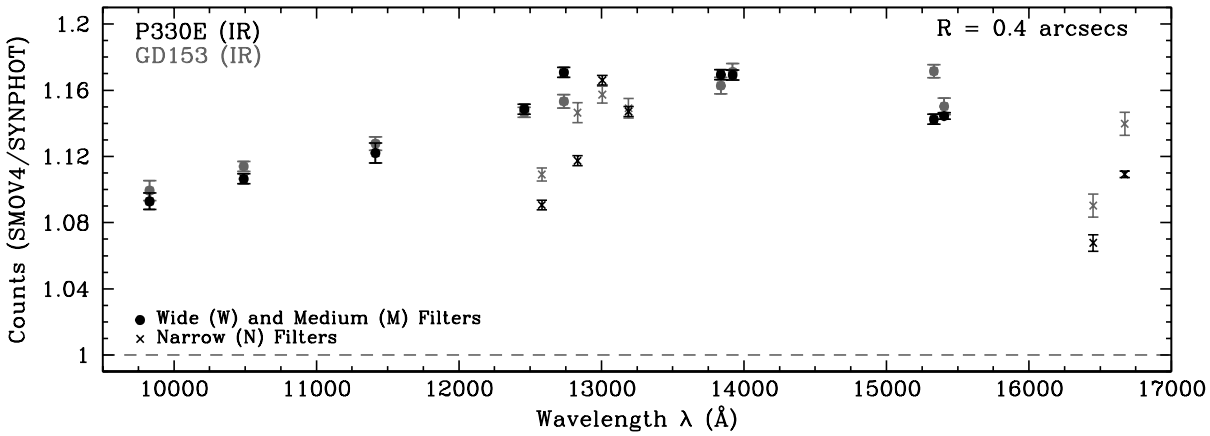

Fig. 4.— *The comparison of our measured photometry for P330E and GD 153 to SYNPHOT predictions that were calibrated based on TV3 ground tests. The photometry for multiple dither positions and epochs has been averaged together, with error bars representing the error in the mean measurements. The medium and wide band filters are plotted as filled circles and the narrow band filters are displayed with crosses, where the darker points represent the P330E observations and the grey points are those for GD 153. Over the entire IR wavelength range, the on-orbit performance of WFC3 is ∼10 – 15% higher than expected based on the ground tests.*

The comparison of SMOV4 observations to SYNPHOT predictions is shown in Figure 4, where we have plotted the medium and wide band filters as filled circles and the narrow band filters as crosses. The darker points represent the P330E observations and the grey points represent the GD 153 data. This comparison illustrates that the true on-orbit system throughput of WFC3/IR is higher than expected from TV3 ground tests. The gain in sensitivity, over all wavelengths is ∼10 – 15%. Further, the independent measurements from the two stars, in almost all of the medium and wide band filters, agree nicely with one another within the uncertainties. The scatter in the narrow band filters is larger, as expected. The uncertainties in the bandpass shape and the wavelengths of the bandpass edges for these filters represent a larger fraction of the integrated area under the throughput curve.

A similar throughput gain was also seen for the UVIS channel of WFC3, as described in Kalirai et al. (2009a). As we discuss in that ISR, the first on-orbit measurements with HST/ACS in 2002 also showed a higher throughput by 2 – 22% vs ground tests (Sirianni et al. 2002). Although these

differences may reflect throughput errors in the detector QEs or other instrument components, another possibility is that a common telescope component is the culprit (e.g., the HST OTA).

7.1 Implementing the New Throughput in SYNPHOT

We follow a similar procedure to that described in Kalirai et al. (2009a) for WFC3/UVIS to implement a correction to the current SYNPHOT count rate predictions for the IR channel. This approach uses an iterative procedure that feeds the current correction into SYNPHOT several times, and compares the resulting synthetic photometry to the observed measurements to define the new correction. The procedure has the advantage that, at each stage, it is the integral of the bandpass with the full system throughput that yields the output photometry (e.g., see De Marchi 2004).

The first step is to remove the TV3 correction that was applied by Brown (2008), which is 2 – 8% depending on the wavelength. The SYNPHOT calculation already included this efficiency gain, and, as we are replacing the SYNPHOT throughput table for the correction factor, we need to multiply our new on-orbit efficiency gain by the existing TV3 correction. Next, a smooth curve that fits the total correction factor (i.e., on-orbit and TV3 combined) is defined, for just the medium and wide band filters. As the two stars P330E and GD 153 yield the same correction, the mean of these two data sets is calculated and the detailed analysis of possible color corrections is left to a later study. The smooth curve is a simple low order (3rd) polynomial. This polynomial is displayed in the top panel of Figure 5, where the dark points represent the P330E observations the grey points are the GD 153 data. Although they are not used in the fit, the narrow band observations are also shown as crosses. This first correction factor is next multiplied into SYNPHOT as a new throughput table, and synthetic photometry is calculated in each of the filters, and again compared to the actual measured photometry. The ratio of these counts is shown in the second panel of Figure 5 and illustrates that the predicted and measured counts now agree to within 2% in all medium and wide band filters. The formal standard deviation in the measurements is 0.74%. This procedure is repeated several times to refine the correction by calculating a new 3rd order polynomial at each stage, and multiplying it by the previous correction. The final standard deviation is 0.30% after the fifth iteration and does not improve with subsequent iterations, thereby defining the final correction factor. Although none of the WFC3/IR filter sensitivities extend to $\lambda \lesssim 9000$ Å, we set the correction factor in the range from 8000 – 9000 Å to the gain seen in the grism observations relative to ground tests (see Kuntschner et al. 2009).

In the bottom panel of Figure 5, we illustrate the ratio of the final SYNPHOT correction from the iterative method described above to the initial polynomial fit in the top panel. Over the bulk of our wavelength range, the iterative approach makes a small (<0.5%) difference in the final correction file, although at our shortest and longest wavelengths the correction can approach 1 – 2%.

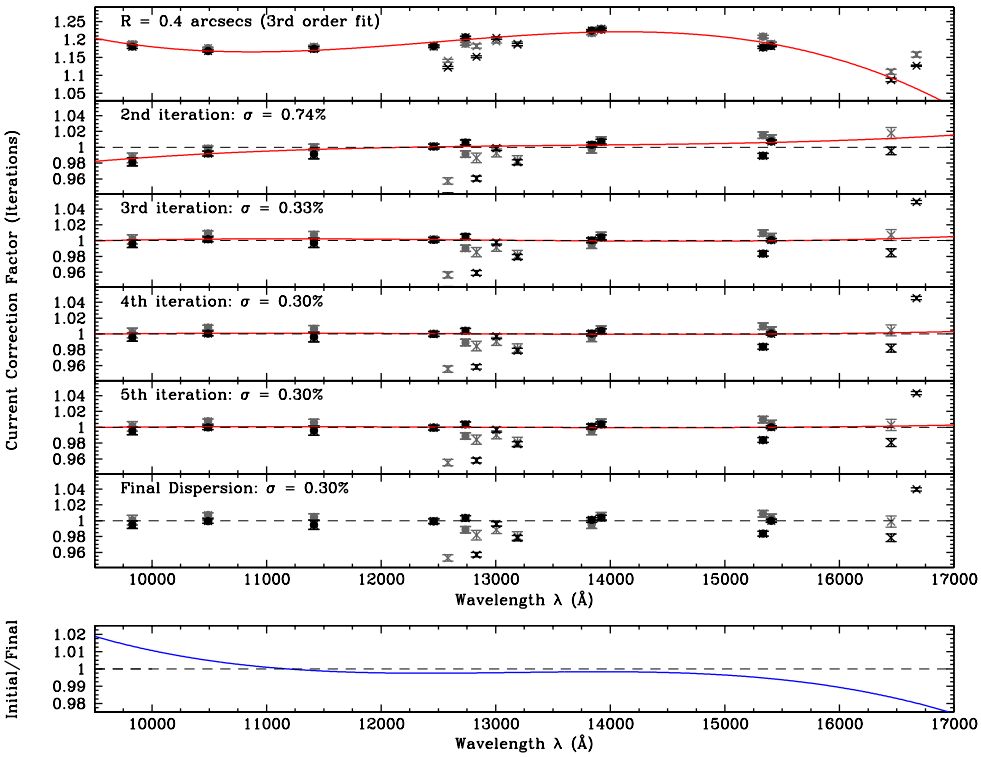

Fig. 5.— *The ratio of our measured on-orbit counts of P330E and GD 153 are compared to SYNPHOT predictions, and a 3rd order polynomial is fit to the mean ratios for the medium and wide band filters for both stars in the top panel (red curve). In each successive panel, we illustrate the resulting comparison between our measured counts and a recalculation of SYNPHOT synthetic photometry with the previous correction factor, which then factors in the integral of the actual bandpass with the (new) full throughput. The new correction is multiplied by the old correction at each step of the iteration, and the measured standard deviation is shown to no longer improve by the 5th iteration. The quoted 0.30% dispersion represents the measurement in all medium and wide band filters. The bottom panel illustrates the ratio of the final SYNPHOT correction to the initial correction displayed in the top panel, showing that the iterative approach makes, at most, a 1 – 2% difference at the blue and red ends of the spectral coverage.*

7.2 Geometric Distortion and Pixel Areas

These data were collected and analyzed prior to the development of a geometric distortion solution for WFC3/IR and, therefore, the analysis was performed on _flt images, which have pixels that vary in their area on the sky. As the sky intensity has been flattened in the calwf3 processed data, the flux in larger pixels on the camera has been suppressed relative to smaller pixels. Therefore, the counts of a given star will vary on the image depending on the spatial position. The magnitude of this effect on WFC3/IR is approximately 8%, going from the bottom to the top of the detector.

In the past (e.g., ACS), photometric zero points have often been defined on drizzled (_drz) images in which the distortion has been removed. The resampled drizzled pixels are flat and uniform in their size. Yet, the input pixel scale for the drizzle process was chosen to be different from the mean native pixel scale of the camera, thereby resulting a global adjustment in the counts within drizzle to account for the differing numbers of pixels sampling any source. As one example of this, the default input scale to drizzle for ACS/HRC is 0.025 arceconds whereas the mean native pixel scale is 0.028 arcseconds. Therefore, the counts on a drizzled ACS/HRC image differ from the input _flt image by ∼12%. To correct this effect, users must multiply _flt images by a pixel area map (PAM) that adjusts that flux to reproduce the drizzled zero points.

For WFC3, we've chosen to adopt a different strategy, one that ensures the same counts will be measured in _flt and _drz images *for a star centered on the detector* (and therefore the same photometric zero point will be applicable to _flt and _drz images). In this case, the normalization of the PAM is set to unity near the center of the detector, and the PAM simply serves to make a relative correction for stars that are not centered. It is the square root of the area of this reference pixel that is set to the input drizzle pixel scale. This choice does not effect the default output pixel scale of drizzle, which can be set to anything users prefer. Specifically for our present purposes of achieving photometric zero points to an accuracy of a few percent, we do not need to apply a PAM correction as the subarray is centered on the detector. Over the 128 pixel range, the pixel areas vary by <1%.[3] For completeness, the reference pixel where the PAM is set to unity is located at (x,y) = (557, 557) and the square root of the area of this pixel is 0.128243 arcseconds. Further details on the WFC3/IR PAM are provided in Kalirai et al. (2009b).

7.3 The Detector Quantum Efficiency

The detector QE of WFC3/IR is illustrated in Figure 6 (e.g., the number of electrons yielded per incident photon). The solid curve illustrates the measured QE of the flight detector (IR4; FPA165) as measured at the DCL at the Goddard Space Flight Center. This represents a significant improvement over previous detectors tested for WFC3. During TV3, Brown (2008) found that the total WFC3 system throughput with this detector exceeded the expectation by 2 – 8%. As the total system throughput involves many components, and the flux calibration of the "CASTLE" system used during the thermal vacuum tests was frequently changed, this difference may be unrelated to the QE. However, if attributed entirely as a QE correction, the new QE would look like the dotted curve. As discussed in the last section, our first on-orbit measurements of the WFC3/IR system throughput indicates a large positive correction on top of the TV3 values. Such a large correction was also seen for WFC3/UVIS (CAL11450 – Kalirai et al. 2009a) and for ACS (Sirianni et al. 2002) and may be partly related to a non-instrument component (e.g., the HST OTA). However, if this

[3]As the PAM is now available, future analysis will still correct for the <1% offset caused by the star not being centered on the reference pixel.

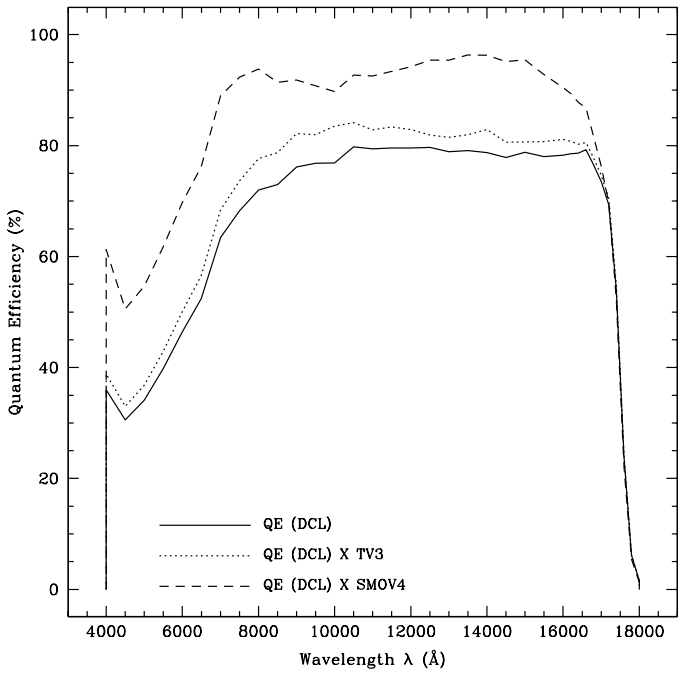

Fig. 6.— *The QE of the IR detector is shown, as measured at the DCL (solid). As discussed in the text, both the TV3 throughput measurements and SMOV4 on-orbit measurements result in a total system efficiency that is higher than expected. The total system throughput represents the convolution of many HST and instrument components (e.g., the OTA, pickoff mirror, filter transmission functions, QE, etc.) and it is not clear what fraction of the throughput gain seen here belongs in the QE. The dotted and dashed lines illustrate what the QE would look like if we attributed 100% of the TV3 and flight corrections as QE enhancements. This clearly results in an unrealistically high QE of >95% at some wavelengths. For the purpose of SYNPHOT throughput calculations, the actual QE of the detector has not been changed; and the measured correction has been folded in as an additional throughput table.*

new correction is entirely assumed to be related to the QE, the updated QE would look like the dashed curve in Figure 6. Given that this new curve approaches 95%, it is highly unlikely that the entire correction belongs in the QE. As discussed earlier, the actual SYNPHOT throughput estimates have been updated by not adjusting the QE, but rather by folding the on-orbit correction factor into an additional throughput table. The overall system throughput in all 15 IR filters is presented in Figure 7.

8. Photometric Zero Points

The photometric zero point of an instrument/filter combination is a convenient way to characterize the overall sensitivity. By most definitions, the zero point represents the magnitude of a star-like object that produces one count per second within a given aperture (see Maiz Apellaniz

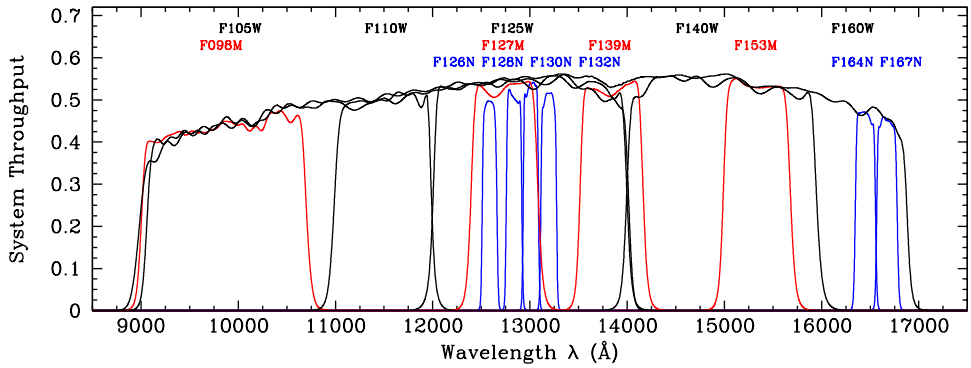

Fig. 7.— *The total system throughput through each of the WFC3 IR filters. The throughput accounts for all telescope and instrument components, as well as the correction factor derived from the first on-orbit observations in this ISR. Further information on these filters is available in the IHB.*

2007). For the present work, the zero points depend on the absolute flux calibration of HST white dwarf spectra, and, therefore, will change whenever that calibration is improved. Following our approach discussed for the WFC3/UVIS calibration (Kalirai et al. 2009a), we calculate photometric zero points both for an infinite aperture (where a small – <3% – model correction extrapolates the measured flux at 2.0 arcseconds to infinity) and for an intermediate aperture of $R = 0.4$ arcseconds. The former can used to determine the zero point in any aperture based on the enclosed energy fractions given in Table 3. We stress that the photometric information in the header of any fits file (e.g., PHOTFLAM) will be the infinite aperture values.

Although the observed magnitude in any WFC3/IR filter is sufficient to define the camera's own photometric system (e.g., WFC3MAG = -2.5log(count rate [e^- s^{-1}]), it is convenient to convert the measured brightnesses into a common photometric system. Among the most popular systems in use today are VEGAMAG, STMAG, and ABMAG, and so we define photometric zero points in each of these systems. These zero points, summarized in Tables 4 and 5, represent additive constants to translate the observed WFC3MAG measurements into the chosen system (e.g., STMAG = -2.5log(count rate [e^- s^{-1}]) + ZP_{STMAG}) and should not be confused with the internal zero points of the system. A brief discussion of these "offsets" is presented in Kalirai et al. (2009a) and a more in depth discussion of the definitions of these photometric systems is given in Sirianni et al. (2005) (see also Maiz Apellaniz 2007). Simply stated, the magnitude of a star in a given photometric system can be calculated by measuring its count rate and adding the zero point from Table 4 or 5.

As discussed in Kalirai et al. (2009a), we discovered an error in the calculation of the SYNPHOT photometric keyword PHOTBW during our analysis. This error currently effects the online tables on the STScI webpage for ACS and are embedded in the headers of most images. The photometric keyword is not used for the zero point calculation, and if required, can be correctly measured

by limiting the wavelength range of the integral that SYNPHOT takes in defining PHOTBW to exclude very blue and red wavelengths.

Table 4: Photometric Zero Points for WFC3/IR, Calculated for an Infinite Aperture

Filter	PHOTFLAM[a]	STMAG	ABMAG	VEGAMAG
F098M	5.974×10^{20}	26.96	25.68	25.12
F105W	3.033×10^{20}	27.70	26.27	25.63
F110W	1.523×10^{20}	28.44	26.83	26.07
F125W	2.213×10^{20}	28.04	26.25	25.35
F126N	4.611×10^{19}	24.74	22.93	22.01
F127M	9.216×10^{20}	26.49	24.65	23.69
F128N	4.103×10^{19}	24.87	23.02	21.98
F130N	3.991×10^{19}	24.90	23.02	22.04
F132N	4.008×10^{19}	24.89	22.98	21.99
F139M	9.059×10^{20}	26.51	24.49	23.42
F140W	1.457×10^{20}	28.49	26.46	25.39
F153M	7.600×10^{20}	26.70	24.46	23.21
F160W	1.911×10^{20}	28.20	25.96	24.70
F164N	2.720×10^{19}	25.31	22.93	21.55
F167N	2.736×10^{19}	25.31	22.89	21.53

[a]PHOTFLAM is the inverse sensitivity; the flux density of a star that produces a response of one count per second in this band pass, measured in ergs cm^{-2} s^{-1} $Å^{-1}$.

9. Summary and Implications

WFC3 is a very powerful high resolution imaging and spectroscopic instrument that allows new scientific discoveries in regimes that HST could not previously probe. Less than three months after its installation, observations with the IR channel of the instrument have already resulted in the discovery and preliminary characterization (e.g., ages and masses) of the highest redshift candidate galaxies known in the Universe (Bouwens et al. 2009a; Oesch et al. 2009a; McLure et al. 2009; Bunker et al. 2009; Oesch et al. 2009b; Bouwens et al. 2009b; Labbe et al. 2009; Yan et al. 2009). Current and future Cycle 17 programs with WFC3/IR will expand our scientific knowledge over a broad range of astrophysical topics, from the formation and evolution of brown dwarf stars, to unprecedented detailed studies of resolved stellar populations in nearby galaxies, to new constraints on the evolution and expansion of the Universe.

The first on-orbit observations of WFC3/IR during SMOV4 demonstrate that the camera is more efficient than expected, exhibiting gains in sensitivity of $\sim$10 – 15% over TV3 tests in the laboratory. Relative to the most sensitive camera on the previous IR instrument on HST, NICMOS, WFC3's absolute throughput is a factor of $\sim$3 – 4 higher and the field of view is >6 times larger than NIC3. The discovery efficiency, defined as the throughput times the area squared, is up to a factor of $\sim$30 larger. The limiting ABMAG magnitude reached for point sources in a 1 hour (10

Table 5: Photometric Zero Points for WFC3/IR, Calculated for $R = 0.4$ arcseconds

Filter	STMAG	ABMAG	VEGAMAG
F098M	26.80	25.52	24.96
F105W	27.53	26.10	25.46
F110W	28.26	26.65	25.89
F125W	27.85	26.06	25.16
F126N	24.55	22.74	21.82
F127M	26.30	24.46	23.50
F128N	24.68	22.83	21.79
F130N	24.71	22.83	21.85
F132N	24.70	22.79	21.80
F139M	26.32	24.30	23.23
F140W	28.30	26.27	25.20
F153M	26.51	24.27	23.02
F160W	28.01	25.77	24.51
F164N	25.11	22.73	21.35
F167N	25.11	22.69	21.33

hour) exposure with WFC3/IR is 27.3 (28.6) in the F110W filter and 26.6 (27.9) in the F160W filter, assuming a S/N = 10 detection.

The improved efficiency of WFC3/IR over expectations has been characterized and folded into the SYNPHOT throughput components and the ETC via a correction factor on top of the existing throughputs. This new throughput file, which is called wfc3_ir_cor_004_syn.fits, replaces a previous file that represented the TV3 correction. All changes have been reflected in the WFC3 pipeline and new photometric keywords in the headers of processed data will provide the updated results. The new component throughput files can be downloaded from the STScI WFC3 reference files webpage.[4]

As summarized in Kalirai et al. (2009c), the SMOV4 observations to characterize WFC3's sensitivity are quite limited. A large Cycle 17 calibration effort will test the longer term stability of the instrument and refine the photometric zero points through the imaging of additional standard stars (e.g., G191-B2B and GD 71). Observations of two star clusters that have been imaged extensively with other HST instruments and ground based telescopes will also be obtained to define photometric transformations between WFC3 filters and other systems.

[4] `http://www.stsci.edu/hst/observatory/cdbs/SIfileInfo/WFC3/reftablequeryindex`

Acknowledgements

We thank the entire WFC3 team for their many years of dedicated effort in producing and calibrating the instrument.

References

Bergeron, P., Saffer, R. A., & Liebert, J. 1992, ApJ, 394, 228
Bohlin, R. C., Colina, L., & Finley, D. S. 1995, AJ, 110, 1316
Bohlin, R. C. 1996, AJ, 111, 1743
Bohlin, R. C. 2000, AJ, 120, 437
Bohlin, R. C., Dickinson, M. E., & Calzetti, D. 2001, AJ, 122, 2118
Bohlin, R. C. 2007a, ACS ISR 2007-06, "Photometric Calibration of the ACS CCD Cameras"
Bohlin, R. C. 2007b, PASP, 364, 315
Bouwens, R. J., et al. 2009a, ApJL, submitted, arXiv:0909.1803
Bouwens, R. J., et al. 2009b, ApJL, submitted, arXiv:0910.0001
Brown, T. M., Reid, I. N., & Figer, D. F. 2005, WFC3 ISR 2005-12, "Results of WFC3 Thermal Vacuum Testing - IR Channel Throughput"
Brown, T. M. 2007, WFC3 ISR 2007-23, "WFC3 TV2 Testing: IR Channel Throughput"
Brown, T. M. 2008, WFC3 ISR 2008-09, "WFC3 TV3 Testing: IR Channel Throughput"
Bunker, A., et al. 2009, MNRAS, submitted, arXiv:0909.2255
Colina, L., & Bohlin, R. 1997, AJ, 113, 1138
De Marchi, G. 2004, ACS ISR 2004-08, "Detector Quantum Efficiency and Photometric Zero Points of the ACS"
Finley, D. S., Koester, D., & Basri, G. 1997, ApJ, 488, 375
Hartig, G., & Dressel, L. 2009, WFC3 ISR 2009 — (CAL11439), in preparation
Hilbert, B. et al. 2009, WFC3 ISR 2009 — (CAL11453), in preparation
Kalirai, J., et al. 2009a, WFC3 ISR 2009-31 (CAL11450), in preparation
Kalirai, J., et al. 2009b, WFC3 ISR 2009 —, in preparation (Pixel Area Maps)
Kalirai, J., et al. 2009c, WFC3 ISR 2009-05, "The Photometric Calibration of WFC3: SMOV and Cycle 17 Observing Plan"
Khozurina-Platais, V. et al. 2009, WFC3 ISR 2009 — (CAL11444), in preparation
Kuntschner, H., et al. 2009, WFC3 TIR 2009 —, "The SMOV Calibration of the WFC3 G102 Grism"
Labbe, I., et al. 2009, ApJ, submitted, arXiv:0910.0838
Maiz Apellaniz, J. 2007, ASP, 364, 227
McLure, R. J., et al. 2009, MNRAS, submitted, arXiv0909.2437
Oesch, P. A., et al. 2009a, ApJL, submitted, arXiv:0909.1806
Oesch, P. A., et al. 2009b, ApJL, submitted, arXiv:0909.5183
Sirianni, M., de Marchi, G., Gilliland, R. L., Bohlin, R. C., Pavlovsky, C., & Mack, J., 2002, HST

Calibration Workshop, 31
Sirianni, M., et al. 2005, PASP, 117, 1049
Stetson, P. B. 1987, PASP, 99, 191
Stetson, P. B. 1994, PASP, 106, 250
Yan, H., et al. 2009, ApJ, submitted, arXiv:0910.0077